A MULTI-SCENE ADAPTIVE CORRECTION AND POSITIONING METHOD FOR MOBILE OPERATION INTEGRATED ROBOT

Chen De*,** Yan Qingdong,* Zhou Junxiong,** Du Yixian,** Wang Hai,** and Li Shipeng***,****

Abstract

The mobile operation integrated robot (MOIR) has the functions of walking freely in the workshop and perform accurate operation by installing actuator. In the practical engineering application, in order to meet the requirements of fast changeover in various working conditions, the end executor needs to have the function of correcting and positioning to achieve the purpose of rapid compatible production online. At present, technical engineers are generally required to operate the camera software, the servo robot software, the end actuator and the corresponding parameters to confirm multiple calibration positions of new products in the production of common industrial robots. Therefore, for practical engineering application, it is urgent to develop an adaptive correcting and positioning (ACP) method with a simple, effective control for real-time implementation. With that in mind, a simple multi-scene ACP method with the advantages of high accuracy, efficiency and reliability in complex work environment was proposed. The pose of the servo robot mounted on the MOIR converting automatically according to the new product size and features under the new working conditions. At the same time, combined with the clarity adaptive recognition algorithm, the system can clearly identify the detection features of the new target object, and store the pose information of the servo robot under the condition of maximum clarity. Finally, practical application experiments are carried out to validate the practicability.

Key Words

Mobile operation integrated robots (MOIR), Adaptive correction and positioning (ACP), Clarity adaptive recognition

* School of Mechanical Engineering, Beijing Institute of Technology, Beijing, China, 100081; email: yanqd@bit.edu.cn
** Guangdong Lyric Robot Automation Co., Ltd, Guangdong, China, 516057
*** China International Marine Containers (Group) Ltd., Guangdong, China, 518118
**** School of Mechanical Engineering, Zhejiang University, Zhejiang, China, 310058
Corresponding author: Yan Qingdong

Recommended by Raffaele Di Gregorio
(DOI: 10.2316/J.2024.206-1042)

1. Introduction

In today's rapidly changing demand, manufacturing enterprises need to quickly respond to the needs of the market, especially for the robot automatic workstation, its flexible, rapid transformation of production is an important technical requirement, so as to meet the changing trend of small batch and multi-category products. Such as to meet the CNC equipment automatic loading and unloading, automatic grinding, automatic palletizing, automatic welding, automatic assembly and other scene requirements. Therefore, after the key elements such as fixture and product dimensions change in the process of transformation, how to quickly realise the automatic transformation of online, automatic correction and positioning is an important research content. In particular, in some production scenarios where there are many types of specifications and the number of each specification is small, the replacement method mainly faces three problems: 1) high skill requirements for operators; 2) teaching operation process is cumbersome; 3) each workpiece needs to be equipped with a set of independent fixture; 4) it takes a long time. For example, in the fields of online appearance defect detection, real-time weld tracking, polishing and polishing in the precise force-position control of precision parts, and automatic assembly of precision parts. After replacing the end effector, it is necessary to carry out online accurate correction and positioning for the new end effector in order to quickly achieve the purpose of accurate control in the production process.

Since this paper is based on a large number of practical applications in the actual production process of smart factories, so far, no identical research objects and corresponding research results have been found.

Lyu *et al.* [1] designed a robot that can autonomously find and pick objects in an unmanned supermarket. Solved the problems of building a robot with both high payload and big workspace and designing a robot system that incorporates the navigation and grasping system. Hao [2] integrated feedforward neural network for mapping the depth image into real-world coordination and convolutional neural network for environment segmentation, proposed a

method for environmental detail mapping and annotation to model. Hanh *et al.* [3] put forward a practical strategy that can significantly reduce the time for a gluing task in footwear industry by using a 6-DOF industrial robot and RGB-D camera. It is challenging to collect enough samples and the collected samples are usually in unbalanced distribution for training in machine learning and computer vision methods. Aimed at those problems, Feng *et al.* [4] employed deep convolution generative adversarial networks (DCGANs) to augment the data and transfer learning method to avoid training from scratch, and the penicillin bottle defects detect experiments result showed the proposed method outperforms the traditional models. Zhang *et al.* [5] proposed a visual servo control system that integrates parallel structure with a wide-angle lens and a telephoto lens, to obtain high-definition images with advantages of more accurate and in good robustness as it can reduce measurement errors. To solve the problem of handling a wide range of object categories need task-specific training data for novel objects, Zeng *et al.* [6] presented a robotic pick-and-place system that can grasp and recognise both known and novel objects in cluttered environments. Wu *et al.* [7] proposed a method for measuring the position and orientation based on monocular vision combined with the 3D model of aerial refuelling drogue target. In order to improve the operational efficiency of robot-based shoe manufacturing, Wu *et al.* [8] proposed a method of shoe-groove tracking based on industrial robot, and some numerical experiments were presented to demonstrate the effectiveness. Abidi *et al.* [9] proposed a new approach to enhance real-world intensity-based visual servoing, with the main goal to direct successfully a robotic task without going through the entire image and improved considerably the computing time. Larouche and Zhu [10] develops a Kalman filter (KF)-enhanced position-based visual servo control strategy for autonomous robotic capture of a moving target with an eye-in-hand-configured robotic manipulator and the efficiency of tracking and capturing of a moving target was improved. Liu *et al.* [11] proposed a novel object-tracking method to provide accurately segmented object boundaries, with the advantages of tracking object with translation, rotation, scale change and partial occlusion. Based on novel monochromatic structured light patterns, Xu *et al.* [12] presented a rapid 3D shape measurement system. By using the two-level fringe patterns to establish the correspondence between the projector image and camera image with sub-pixel accuracy, and overcome the occlusion to achieve high density measurement. Siradjiddin *et al.* [13] presented a distributed fuzzy proportional control system for a vision-guided redundant robot manipulator to track moving objects through a variety of motions without a priori knowledge of the robot kinematic. Zhao and Wang [14] devised a binocular stereo vision measurement system with two CCD cameras to obtain the images of a detected object's 3D surface boundary, presented a novel measurement scheme for a three-dimensional object's surface boundary perimeter and a bent surface's perimeter measurement indicated the repetition error decreases to 0.6%. To compensate for the unknown camera calibration parameters, a novel prediction error formulation was presented by Tatlicioglu *et al.* [15], realised image-based regulation control of a robot manipulator with an uncalibrated vision system. By employing the pseudo stereovision system (PSVS) to capture a complex image in a single shot, Pachidis and Lygouras [16] proposed a vision-based path generation method for a robotic arc welding system that no need to "Teaching by Showing" like method. By using structured light 3D machine vision for object profile perception, and NURBS interpolation for accurate and smooth trajectory generation, Hu *et al.* [17] proposed an innovative and practical strategy for automated leather surface roughing. Fang *et al.* [18] proposed a new class of model-free (*i.e.*, the three-dimensional task-space model of the object is unknown) visual servoing method to realise the estimation of the relative camera orientation between two views of an object. Bender and Bone [19] presented an automated grasping system suitable for complex 2.5D real-world objects (*i.e.*, objects with height $<$ width), which consists of a robotic manipulator, a three-fingered dexterous hand with a palm-mounted CCD camera, and a PC. The advantages of precise and efficiency were verified by some experiments of grasping three complex-shaped automotive parts. Paul *et al.*[20] applied visual servoing mechanisms for handling objects and camera calibration and object inspection and proposed an image-based effector servoing method to handle cylindrical and cuboid pegs.

Visual serving technology has made some progress in research and has application experience in some fields. Visual serving is mainly used in known and determined detection and tracking objects, but in the application process, it needs to calibrate the artificial hand-eye system for each determined detection and following object, which consumes a lot of time and leads to the decrease of production line output, so the practical application value is low. However, for the multi-variety, small-scale detection and tracking scenarios of fully automated production lines, especially for the application conditions requiring frequent and rapid type change detection and unknown detection objects, visual serving is powerless.

Aiming at these problems, this paper presents an online multi-scene adaptive correction and positioning (ACP) strategy combined with the clarity automatic recognition algorithm for the mobile operation integrated robot (MOIR). To realise the function of online automatic displacement production of MOIR in the field of multi-variety and small-batch production, and quickly and accurately realise the automatic displacement of end-effector. Thus, greatly shorten the time of automatic replacement, improve production efficiency, and meet the needs of rapid compatible production of automatic production lines in smart factories.

The remainder of this paper is organised as follows. In Section 2, the proposed method is described. Practical application experimental studies are presented in Section 3. Section 4 includes the experimental results and analysis. Finally, discussion and conclusions are provided in Section 5.

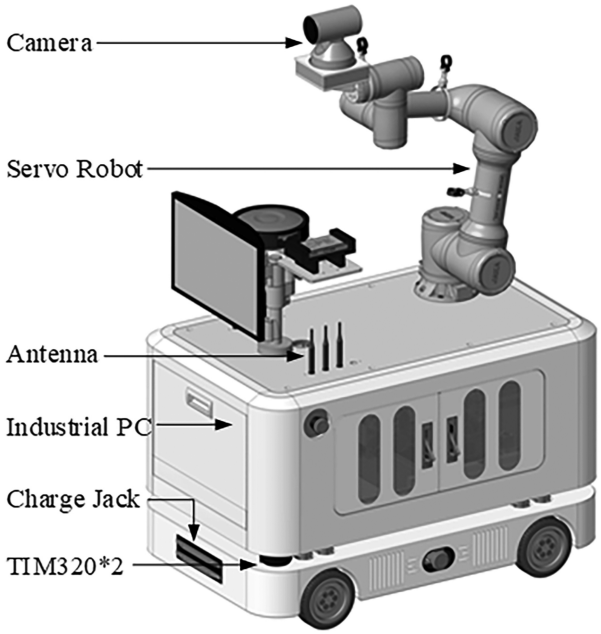

Figure 1. Mechanical design of MOIR.

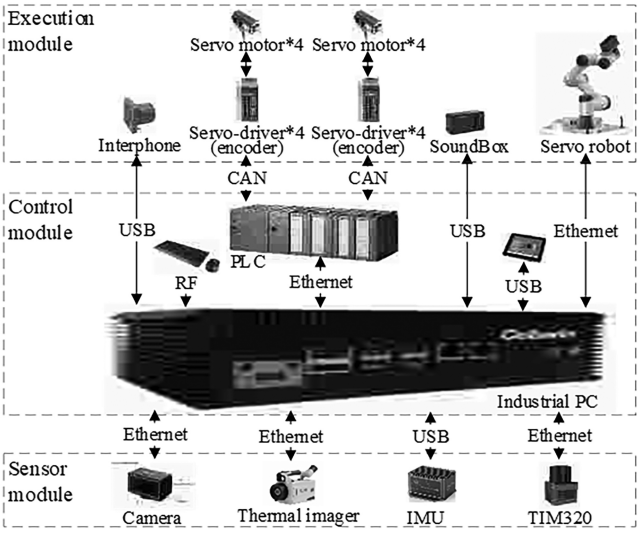

Figure 2. Electrical design schematics of MOIR.

2. Multi-scene ACP Method

2.1 System Description

As shown in Fig. 1, the dimension of the MOIR is approximately 900 mm × 500 mm × 950 mm. Four driving wheels were mounted on the left and right sides of the MOIR and were driven by four servo motors, and the four driving wheels can achieve independent steering function to meet the goal of flexible operation in narrow spaces of the semi-open industrial scenarios. The laser navigation system SICK TIM320 was mounted as the positioning sensor with an accuracy of ±20 mm. An industrial PC was used as the main controller and a touch screen monitor was used for providing the input, and a lithium battery pack was mounted inside the MOIR to supply power. In addition, a servo robot with a camera attached to the end was installed on the top. Fig. 2 shows the MOIR electrical design schematic. Critical modules included the sensor module, control module, and execution module. Four encoders were used for landmark detection and obstacle detection and two LiDARs of SICK TIM320 for measuring the absolute coordinates.

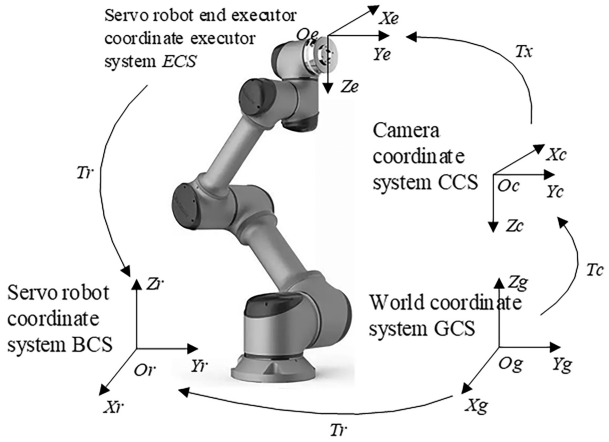

Figure 3. The relationship between coordinate systems.

2.2 Visual System Calibration

The servo robot mounted on the MOIR has a camera and an end executor at the end. In the hand-eye calibration system, four coordinate systems are mainly involved: the servo robot coordinate system BCS, the servo robot end coordinate system ECS, the camera coordinate system CCS and the world coordinate system GCS. Figure 3 shows the relationship between coordinate systems. The world coordinate system GCS is usually determined by the pose of the calibration plate during the camera calibration process.

2.3 Camera Calibration and Servo Robot Modelling

2.3.1 Camera Calibration Method

The purpose of camera calibration is to establish the transformation relationship between the image coordinate system and robot coordinate system. The process of camera calibration method adopted in this paper is shown in Fig. 4, the main steps can be explained as follows:

Step 1: Get calibration images. The camera obtains 3–5 images of the nine-point calibration plate, according to the sequence as shown in Fig. 5.

Step 2: Extract features and calculate rotation center. The system extracts feature points and refines subpixels according to the images. Suppose (r_{x0}, r_{y0}) is the center of rotation, (x, y) is the point to be rotated, and (x_0, y_0) is the rotated point, then the rotation center point can be expressed as:

$$\begin{cases} x_0 = \cos(\alpha) * (x - r_{x0}) - \sin(\alpha) * (y - y_{y0}) + r_{x0} \\ y_0 = \cos(\alpha) * (y - r_{y0}) - \sin(\alpha) * (x - y_{x0}) + r_{y0} \end{cases} \quad (1)$$

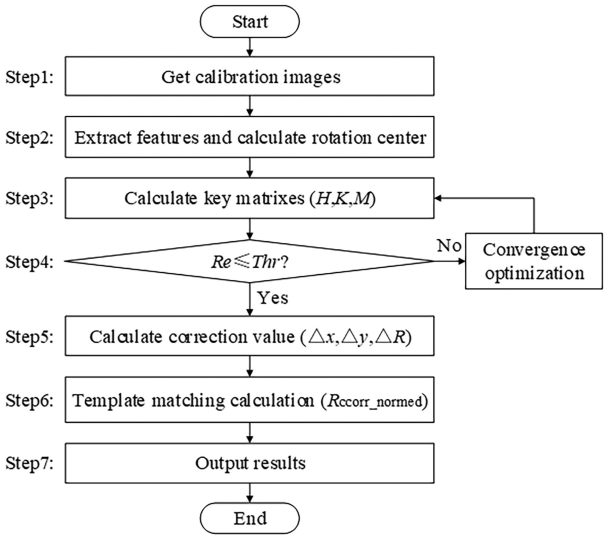

Figure 4. The process of camera calibration method.

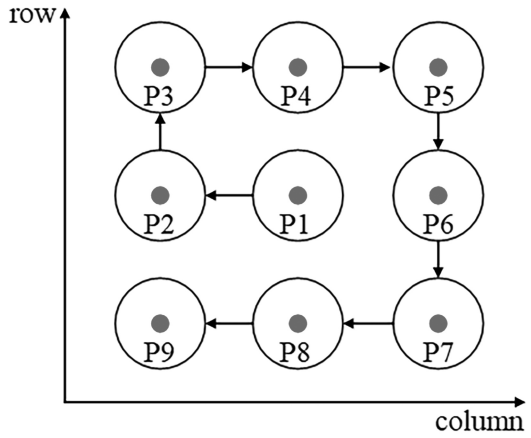

Figure 5. Nine-point calibration sequence.

Step 3: Calculate key matrixes. Calculate the unit matrix H, the internal parameter matrix K and the external parameter matrix M of the camera.

Step 4: $Re \leq Thr$? Calculate the reprojection error Re, preset a threshold value Thr, and judge whether Re is less than or equal to Thr or not. If so, turn to step 5 and continue the modelling process until it complete; otherwise, the convergence optimisation will be carried out and return to step 3 and continue the calibration.

Step 5: Calculate the correction values $(\Delta x, \Delta y, \Delta R)$. As shown in Fig. 6, set the position after correction as (x_1, y_1, R_1), then the angle deviation ΔR between the current position (x, y, R) and the template position (x_m, y_m, R_m) can be written as:

$$\Delta R = R_m - R \tag{2}$$

Then the position after correction according to the central rotation point (x_c, y_c, R_c) can be expressed as:

$$\begin{cases} x_1 = (x - x_c) * cos(\Delta R) - (y - y_c) * sin(\Delta R) \\ y_1 = (x - x_c) * sin(\Delta R) + (y - y_c) * cos(\Delta R) \end{cases} \tag{3}$$

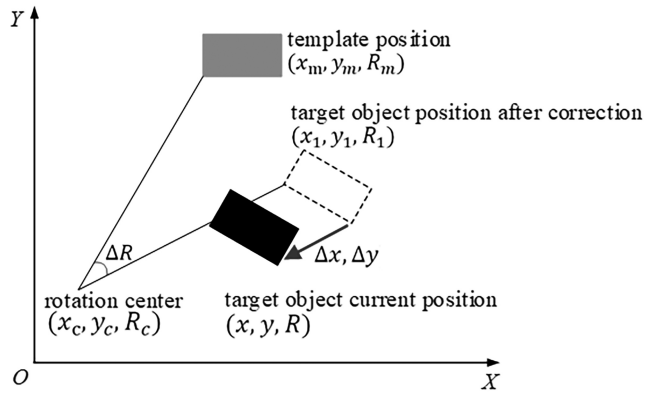

Figure 6. The diagram of rectification principle.

And the position deviation after the shift can be written as:

$$\begin{cases} \Delta x = x_m - x_1 \\ \Delta y = y_m - y_1 \end{cases} \tag{4}$$

Step 6: Template matching calculation. Template matching is one of the core functional modules in the algorithm proposed in this paper. The stability of the process directly determines the accuracy and stability of the ACP method. Suppose that $f(x, y)$ and $t(x, y)$ are the original image and the template, respectively, the enhanced image after convolution calculation is $g(x, y)$, then the convolution formula can be written as:

$$g(x, y) = f(x, y) \circ t(x, y) \tag{5}$$

The discrete convolution formula of (5) can be defined as follows:

$$g(x, y) = \sum_{m=1}^{M} \sum_{n=1}^{N} t(m, n) \cdot f(i - m, j - n) \tag{6}$$

Where M and N are the dimensions of the template.

As (7) shows, normalised correlation matching is carried out between the preprocessed template image and the detected image, and the coordinates with the highest degree of matching are returned.

$$R_{\text{ccorr\_normed}} = \frac{\sum_{x'y'} T(x', y') \cdot I(x + x', y + y')}{\sqrt{\sum_{x'y'} T(x', y')^2 \cdot \sum_{x'y'} I(x + x', y + y')^2}} \tag{7}$$

Where $T(x', y')$ and $I(x, y)$ are the template matrix and the original image matrix, respectively. R is the result value obtained from the calculation matrix, and the best matching result can be obtained when the value of R is maximum.

Step 7: Output results then end the calibration process.

2.3.2 Servo Robot Modelling Method

The servo robot modelling is the first modelling of the extraction point and the photo point, so as to adapt to the

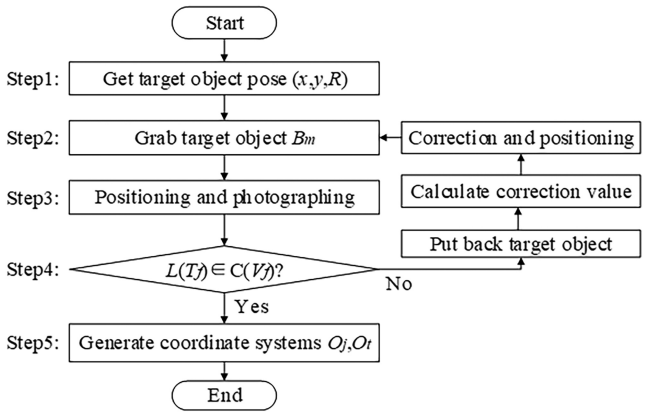

Figure 7. Servo robot modelling process.

correction and positioning of different types of products during the automatic transformation process. Figure 7 shows the modelling flowchart of the servo robot in this paper. The main steps are described as:

Step 1: Get target object pose. The camera acquires the pose information (x, y, R) of the target object and feeds it back to the control system and the servo robot system.

Step 2: Grab target object. The servo robot of MOIR grabs the target object B_m according to the result of step 1.

Step 3: Positioning and photographing. The servo robot of MOIR completes the positioning of the target object, and the camera system starts photo program to obtain the corresponding images.

Step 4: $L(T_f) \in C(V_f)$? Determine whether the target features are at the view field center. Suppose $L(T_f)$ contains all of the target features locations, and $C(V_f)$ is the view field center. Then two cases in this step, that is, if the target features locate in the vision field center, turn to Step 5 and continue the modelling process until it complete. Otherwise, the servo robot will put back the target object then calculate the correction and positioning information, and send it to the control system, which controls the end executor of the servo robot to correct the pose deviation. Then return to Step 2 and continue the modelling process.

Step 5: Generate coordinate systems. If the target features locate in the vision field center, generate the first workpiece coordinate system O_j and the first tool coordinate system O_t, then end the modelling process.

2.4 Clarity Automatic Recognition Algorithm

In order to automatically obtain the pose information of each joint of the servo robot during the ACP, it is necessary to carry out automatic imaging clarity calculation on the target object. Figure 8 shows the adaptive clarity calculation flow. Table 1 is the corresponding pseudocode. The clarity calculation process is mainly divided into eight steps, and each step can be explained as follows:

Step 1: Convert the RGB image I_{rgb} to gray image I_{gray}. In order to improve the accuracy of image conversion calculation, this paper optimises by converting floating-point arithmetic into integer arithmetic and integer

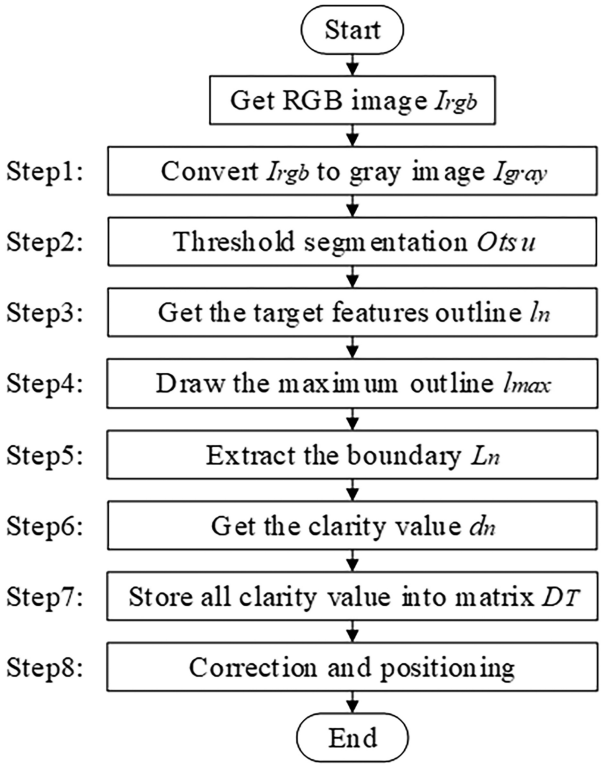

Figure 8. The diagram of adaptive clarity calculation.

arithmetic into bit arithmetic.

$$Grey = (299 * R + 587 * G + 114 * B + 500) / 1000 \quad (8)$$

Where R, G and B are the three components of each pixel in RGB image; since integer arithmetic truncates the decimal part, 500 is added to the end of the equation to reduce precision loss.

Step 2: **T**hreshold segmentation. Otsu threshold method is used to segment the target (black) and background (white) in the whole image. Set the grey level of the image is L and the number of pixels with gray level as i is n_i, then the histogram distribution of the image is:

$$p_i = \frac{n_i}{N}, \quad \sum_{i=0}^{L-1} p_i = 1 \quad (9)$$

According to the grey level, the threshold value t can be divided into two classes, that is $C_0 = (0, 1, \ldots, t)$, and $C_1 = (t+1, t+2, \ldots, L-1)$. The mean probability levels of class C_0 and class C_1 are, respectively, as:

$$w_0 = P_r(C_0) = \sum_{i=0}^{k} p_i \quad (10)$$

$$w_1 = P_r(C_1) = \sum_{i=k+1}^{L-1} p_i = 1 - w_0 \quad (11)$$

$$u_0 = \sum_{i=0}^{k} i * P_r(i|C_0) = \sum_{i=0}^{k} i * p_i / w_0 \quad (12)$$

$$u_1 = \sum_{i=k+1}^{L-1} i * P_r(i|C_1) = \sum_{i=k+1}^{L-1} i * p_i / w_1 \quad (13)$$

Table 1
Pseudocode of the Adaptive Clarity Calculation

Algorithm:	Adaptive clarity calculation algorithm
Input:	RGB pictures
Output:	[the maximum clarity value $d_{\max}$, the pose information $(x_T, y_T, z_T, \alpha_T, \beta_T, \gamma_T)$]
Calculation:	
1:	Start and input RGB image I_{rgb};
2:	Convert I_{rgb} to gray image I_{gray};
3:	Clip the gray image I_{gray}, and get the target area ROI;
4:	Segment the ROI region by Otsu threshold algorithm;
5:	Eliminate small areas with Opening operations in morphology;
6:	Put all sub-contours into the sub-contours set $O = \{o_1, o_2, \ldots, o_n\}$;
7:	*for* $o_i \in O$ do
8:	$a_i \leftarrow$the area of the sub-contour o_i; $A_T = \{a_1, a_2, \ldots, a_n\}$, store all a_i into matrix A_T
9:	*for* $a_i \in A_T$
10:	*if* $a_i > a_{\max}$(the threshold value of the maximum sub-contour area)
11:	$a_{\max} = a_i$;
12:	*end if*
13:	*end for*
14:	*end for*
15:	*patch_img* $\leftarrow$ Grab the region containing the target area;
16:	$d_i \leftarrow$get the resolution value of *patch_img* using the *Laplacian* operator; $D_T = \{d_1, d_2, \ldots, d_n\}$, store all d_i into matrix D_T;
17:	*for* $d_i \in D_T$ do
18:	*If* $d_i > d_{\max}$(the threshold value of the maximum resolution)
19:	$d_{\max} = d_i$;
20:	*end if*
21:	*end for*
22:	$(x_T, y_T, z_T, \alpha_T, \beta_T, \gamma_T) \leftarrow$store the pose information of the servo robot control system;
23:	Feed pose information $(x_T, y_T, z_T, \alpha_T, \beta_T, \gamma_T)$ back to the servo robot control system.

$$u_T = \sum_{i=0}^{L-1} i * p_i \tag{14}$$

$$w_0 u_0 + w_1 u_1 = u_T, w_0 + w_1 = 1 \tag{15}$$

The variance of class C_0 and class C_1 are, respectively, as:

$$\sigma_0^2 = \sum_{i=0}^{t} (i - u_0)^2 * p_i / w_0 \tag{16}$$

$$\sigma_1^2 = \sum_{i=t-1}^{L-1} (i - u_1)^2 * p_i / w_1 \tag{17}$$

Then the intraclass variance and the interclass variance can be, respectively, expressed as follows:

$$\sigma_W^2 = w_0 \sigma_0^2 + w_1 \sigma_1^2 \tag{18}$$

$$\sigma_B^2 = w_0 (u_0 - u_t)^2 + w_1 (u_1 - u_t)^2 = w_0 w_1 (u_1 - u_0)^2 \tag{19}$$

$$\sigma_T^2 = \sigma_B^2 + \sigma_W^2 \tag{20}$$

So the grey level L is reflected in the histogram as two types of grey. What we need to do is to find the maximum threshold to make the difference between the two kinds of grey, according to which the grey image is segmented. So the aim is to find the applicable value of t that maximised the variance between classes.

Step 3: Get the target features outline l_n. This paper employed Harris corner detection algorithm to calculate the sub-contours of the target features, and its mathematical expression is as follows:

$$E(u,v) = \sum_{x,y} w(x,y)\left[I(x+u,y+v) - I(x,y)\right]^2 \quad (21)$$

Where $E(u,v)$ is the energy function, (u,v) is the shift step of window; (x,y) is the coordinates of pixel points; and $w(x,y)$ is the weight of pixel-value differencing which represent the current pixel contribution to the whole calculation, and can realise by median filtering or Gaussian filtering. $I(x+u,y+v)-I(x,y)$ is the grey difference before and after the window shift.

Step 4: Draw the maximum outline $l_{\max}$. The Green formula was adopted to calculate the area of each sub-contour. It can be written as:

$$S = \iint_d (\frac{\partial Q}{\partial x} - \frac{\partial P}{\partial y}) d_\sigma = \oint_L P d_x + Q d_y \quad (22)$$

Where $P(x,y)$ and $Q(x,y)$ are in the region of D, L and S are the positive boundary curve and the area of sub-contour region D, respectively.

Step 5: Extract the boundary L_n.

1) The Laplacian operator module is used to compute the gradient of image, that is, for two-dimensional image $f(x,y)$, the Laplacian operator is defined as:

$$\nabla^2 f = \frac{\partial^2 f}{\partial x^2} + \frac{\partial^2 f}{\partial y^2} \quad (23)$$

In order to be more suitable for digital image processing, (23) can be expressed in discrete form:

$$\begin{aligned}\Delta^2 f = &[f(x+1,y) + f(x-1,y) + f(x,y+1) \\ &+ f(x,y-1) - 4f(x,y)]\end{aligned} \quad (24)$$

2) Calculate the grey value gradient

We employed the second derivative of Laplacian operator to emphasise the detection of boundary regions with rapidly changing density in the image. For each pixel in the image, the square of grey difference between two adjacent pixels is calculated according to (25):

$$D(f) = \sum_y \sum_x |f(x+2,y) - f(x,y)|^2 \quad (25)$$

Where $f(x,y)$ represents the grey value of the pixel (x,y) of image f, and $D(f)$ represents the image clarity value. According to the above analysis, the larger the $D(f)$ value is, the clearer the image will be.

Step 6: Get the clarity value d_n. In general, a normal image with clear boundaries will have a larger variance, while a fuzzy image contains less boundary information, so the variance will be smaller. For a fuzzy image, the grey value near each pixel changes little, then the gradient value is also small; while for a clear image, the image outline is sharp, the gradient value will be large. Based on this analysis, in order to speed-up the calculation efficiency, the convolution kernel shown in Fig. 9 is employed as the Laplacian filter convolution for scanning calculation to obtain the maximum clarity value.

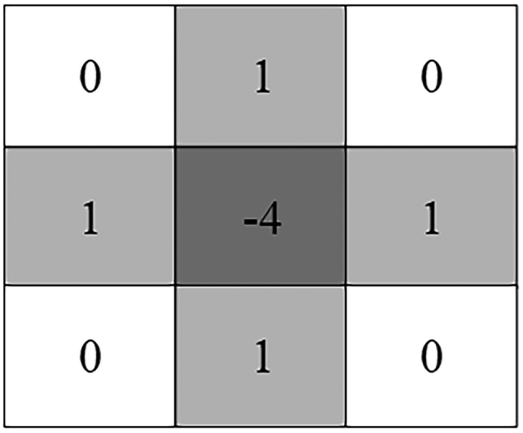

Figure 9. The Laplace filter convolution kernel.

Step 7: Store all clarity value d_n into matrix D_T, and pick the pose information $(x_T, y_T, z_T, \alpha_T, \beta_T, \gamma_T)$ that meet the maximum clarity value and feed it back to the servo robot control system. The way to get the maximum clarity value can be expressed as follows:

$$D_T = [d_1, d_2, ..., d_n] \quad (26)$$

$$d_{\max} = \max[D_T] \quad (27)$$

Where d_n represents the n-th clarity value, and $d_{\max}$ is the largest clarity value of the matrix D_T.

Step 8: Correction and positioning. The servo robot of the MOIR correction and positioning according to the pose information $(x_T, y_T, z_T, \alpha_T, \beta_T, \gamma_T)$.

2.5 Evaluation Method

Two evaluation indexes were proposed to verify the reliability, stability and compatibility of the proposed method in this paper, namely, the repeated correction and positioning evaluation method and the compatible correction and positioning evaluation method.

2.5.1 Repeated Reliability Evaluation Methods

It is assumed that the same target object has N detection points. Under the same test conditions, the MOIR should correction and positioning N times for each target object, and repeat the detection for W times, then the repeated reliability evaluation of the same target object is defined as:

$$R_{\text{it}} = \frac{\sum_{t=1}^{W}(d_{\text{it}})}{W \times T_i}, (i = 1,2,...,N; t = 1,2,...,W) \quad (28)$$

$$R_{\text{it}} \geq R_{\text{iD}} \quad (29)$$

Where R_{it} is the accuracy of repeated correction and positioning at the i-th detection point, d_{it} is the clarity value of the i-th detection point and the t-th time. T_i is the target clarity value of the i-th point. R_{iD} is the reliability evaluation threshold of the i-th detection point in the same target object.

Then the system repeated reliability of the same target object is defined as:

$$R_{\mathrm{rsd}} = \frac{\sum_{i=1}^{N}(R_{\mathrm{it}})}{W}, (i = 1, 2, ..., N; t = 1, 2, ..., W) \quad (30)$$

$$R_{\mathrm{rsd}} \geq R_D \quad (31)$$

Where R_{rsd} is the system repeat reliability accuracy of N detection points by W times in the same target object; R_D is the system repeat reliability accuracy threshold, the value is determined by the pixel of the imaging system and the accuracy requirements of the detection condition.

2.5.2 Compatible Reliability Evaluation Method

Suppose that there are M kinds of target objects, and each of them has N detection points. Under the same test conditions, the MOIR carries out the correction and positioning of M kinds target objects in turn, and records the clarity value d_{ab} of the target object during the correction and positioning, respectively. Then the system compatible correction and positioning evaluation of the target object a and detection point b is defined as:

$$R_{\mathrm{ab}} = \frac{\sum_{b=1}^{M}(d_{\mathrm{ab}})}{M \times T_{\mathrm{ab}}}, (a = 1, 2, \ldots, M; b = 1, 2, \ldots, N) \quad (32)$$

$$R_{\mathrm{ab}} \geq R_{\mathrm{abD}} \quad (33)$$

Where R_{ab} is the system compatible accuracy of target object a and the b-th detection point; T_{ab} is the target clarity value of target object a and the b-th detection point; R_{abD} is the system compatible reliability evaluation threshold of target object a and the b-th detection point.

Then the system compatible reliability of M kinds of target objects is defined as:

$$R_{\mathrm{comp}} = \frac{\sum_{a=1}^{N}(R_{\mathrm{ab}})}{M}, (a{=}1, 2, \ldots, M; b{=}1, 2, \ldots, N) \quad (34)$$

$$R_{\mathrm{comp}} \geq R_C \quad (35)$$

Where R_{comp} is the system compatible reliability accuracy of N detection points by W times in M kinds of target objects, and R_C is the system compatible reliability accuracy threshold, and the value is determined by the pixel of the imaging system and the accuracy requirements of the detection condition.

3. Practical Application Experiments Introduction

As indicated in Figs. 10–12, some practical application experiments are performed in this section to validate the ACP technique developed in this paper, namely, the ACP function test, the repeated reliability evaluation test and the compatible reliability evaluation test. Figure 10 shows the experimental scene, Fig. 11 is the actual experimental scenario. Here the purpose of the test platform mainly realises the hem process of lithium-ion battery cells and the appearance defect detection of finished battery cells.

The proposed method will be applied to 50 kinds of lithium-ion battery cells (as Fig. 12 shows, numbered$[B_1, B_2, \cdots B_{50}]$) on 8 MOIRs (numbered

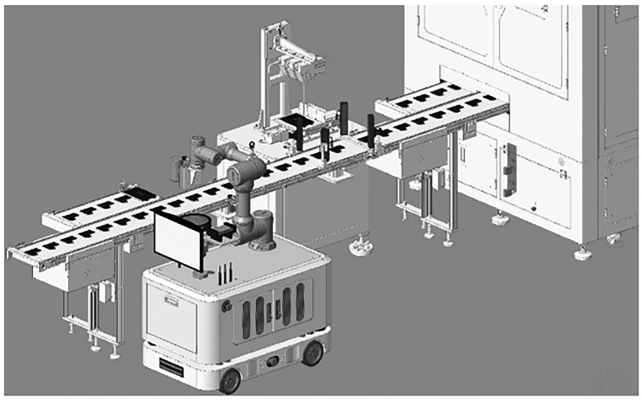

Figure 10. The diagram of MOIR follows detection online.

Figure 11. Actual situation of the production line.

$[R_1, R_2, \ldots R_8]$). As Fig. 13 shows, each kind of lithium-ion battery cells contains 7 detection points, that is, the left corner (CL), the right corner (CR), the long side 1($L1$), the long side 2 ($L2$), the left head (HL), the right head (HR) and the tail (TW).

Figure 14 shows partial process of adaptive correction of the servo robot, and Fig. 15 shows partial process of adaptive calibration of the camera.

Before the ACP, the servo robot needs to get the correction information $(\Delta x, \Delta y, \Delta R)$ of each lithium-ion battery cell by the camera attached at the end of the servo robot, as the shape and orientation of lithium-ion battery cells upstream of the automated production line are different. Figure 16 shows some experimental results with correction information $(\Delta x, \Delta y, \Delta R)$ of different lithium-ion battery cell types before ACP. Then the servo robot will grab the object, correct the end executor's pose according to the correction information as mentioned above, and move to the target photo position automatically. Then the end executor of the servo robot will carry out vertical movements of 5 mm up and down with lithium-ion battery cells based on the height of the target photo location. During the movements, the camera system will take pictures at 0.5 mm intervals, and the clarity recognition algorithm proposed in this paper will be performed after every photograph. The upper computer system will make a comparative analysis according to the clarity values of the current type of lithium-ion battery cell, and

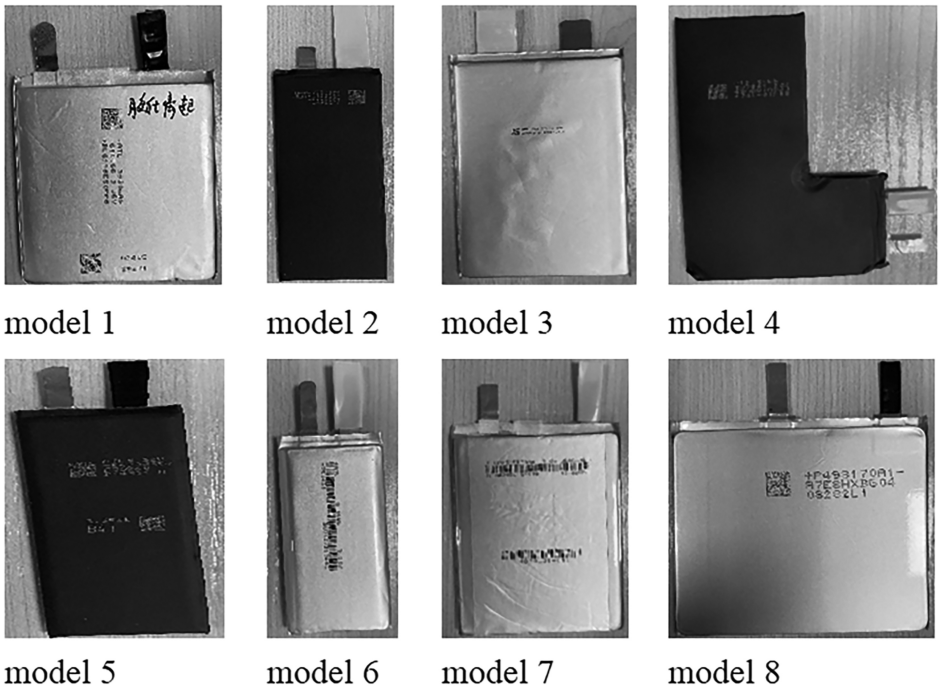

Figure 12. Partial models of lithium-ion battery cells: (a) model 1; (b) model 2; (c) model 3; (d) model 4; (e) model 5; (f) model 6; (g) model 7; (h) model 8.

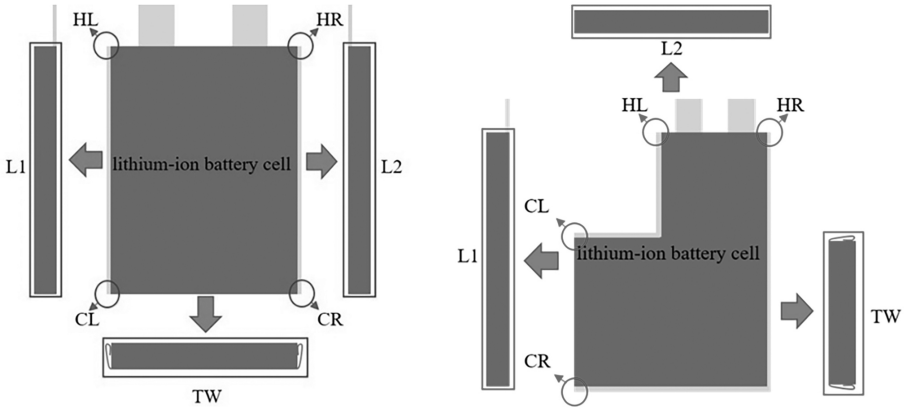

Figure 13. Lithium-ion battery cell structure diagram (the "I" model and the "L" model).

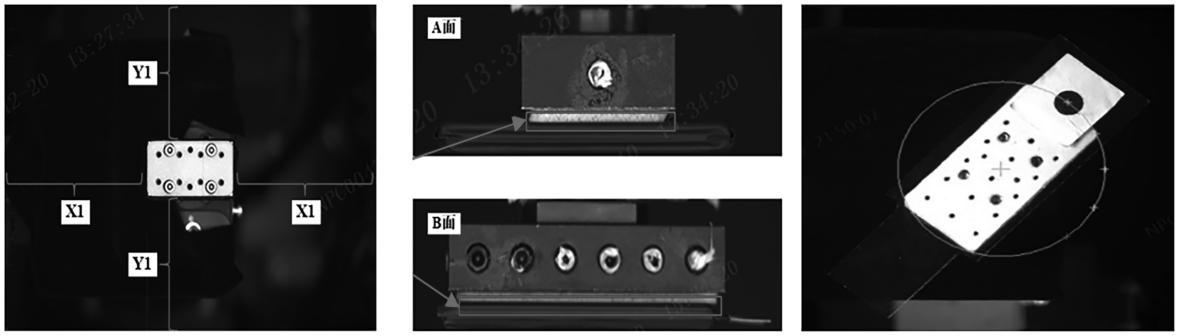

Figure 14. Partial process pictures of adaptive correction of the servo robot.

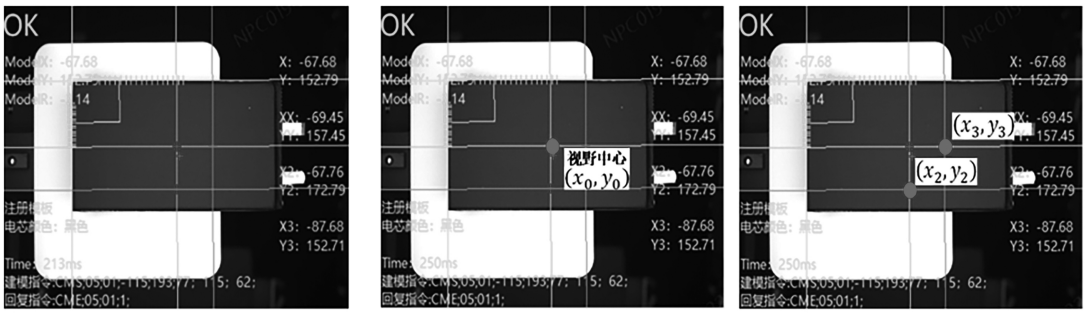

Figure 15. Partial process pictures of adaptive calibration of the camera.

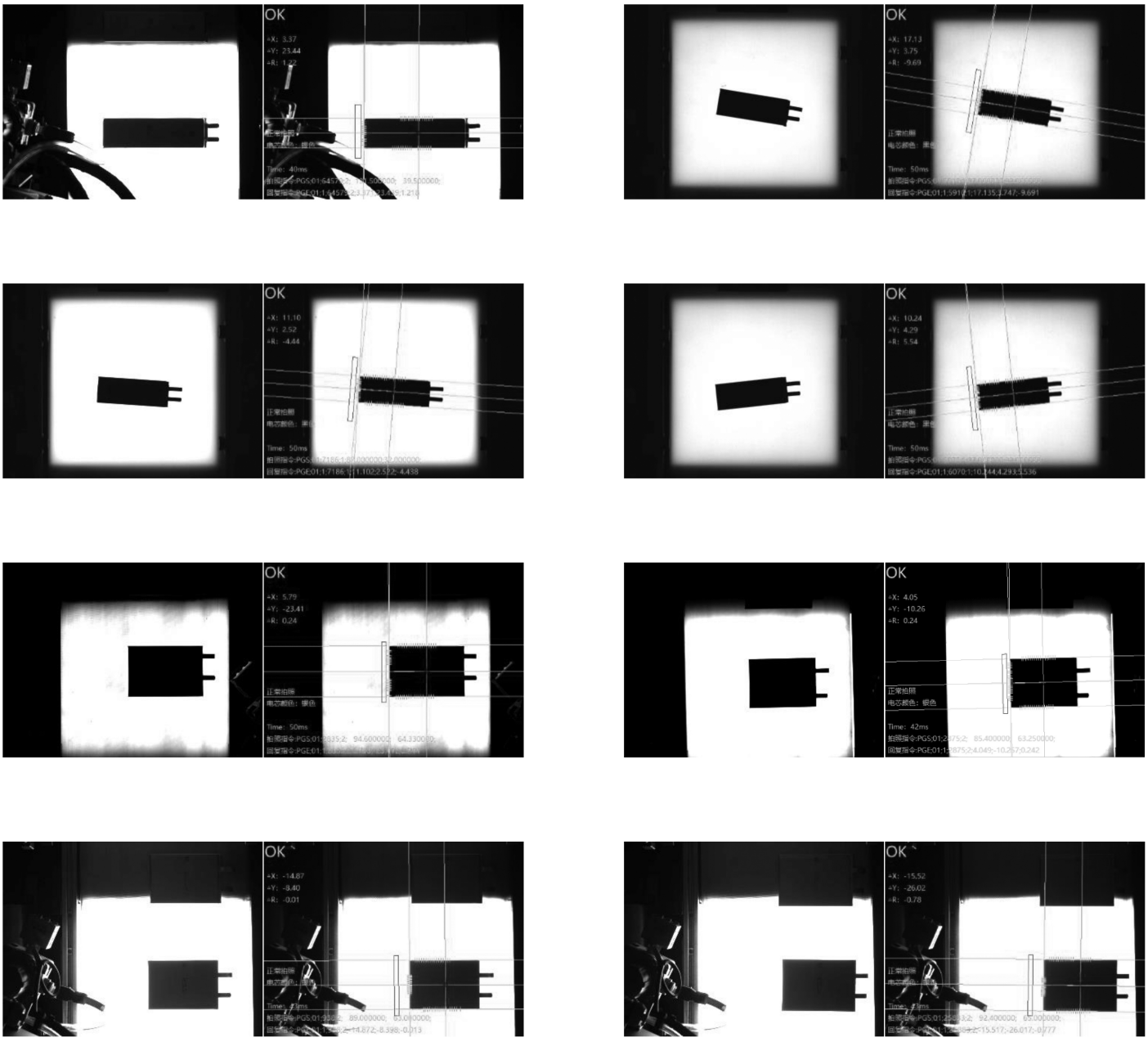

Figure 16. Some experimental results with correction information $(\Delta x, \Delta y, \Delta R)$ of different lithium-ion battery cell types (before ACP).

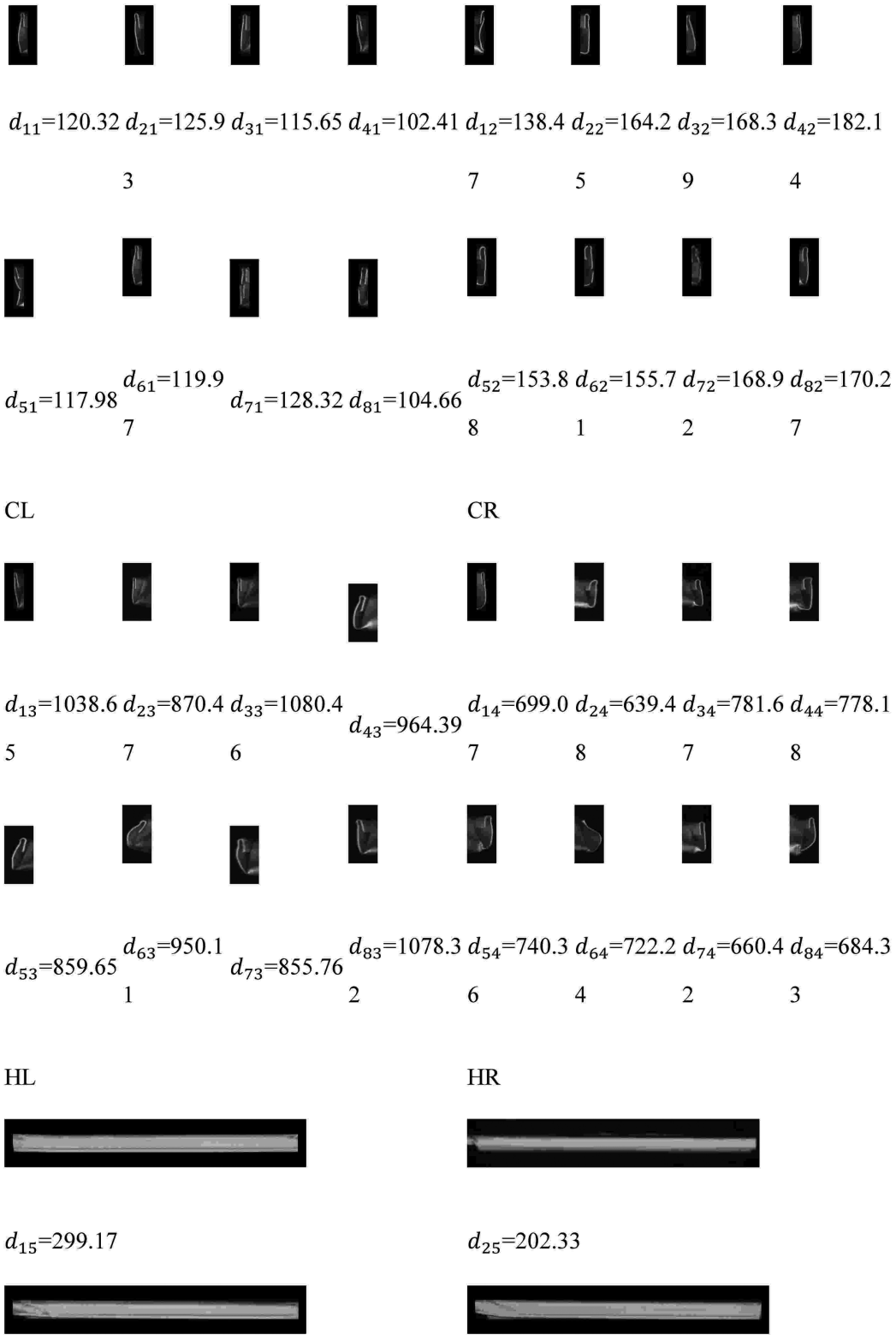

Figure 17. Some experimental results with clarity value d_{ab} of different detection positions (after ACP).

select the parameter information $(x_T, y_T, z_T, \alpha_T, \beta_T, \gamma_T)$ corresponding to each degree of freedom of the servo robot when the clarity value is maximum. Record and save the corresponding parameter information for real-time ACP in the mass production process. Figure 17 shows some experimental results with clarity value d_{ab} of different detection positions after ACP.

4. Experimental Results and Analysis

4.1 Automatic Transformation Results Analysis

In order to verify the multi-scene ACP function proposed in this paper, an MOIR numbered R_1 was used to carry out automatic transformation tests on 50 kinds of battery

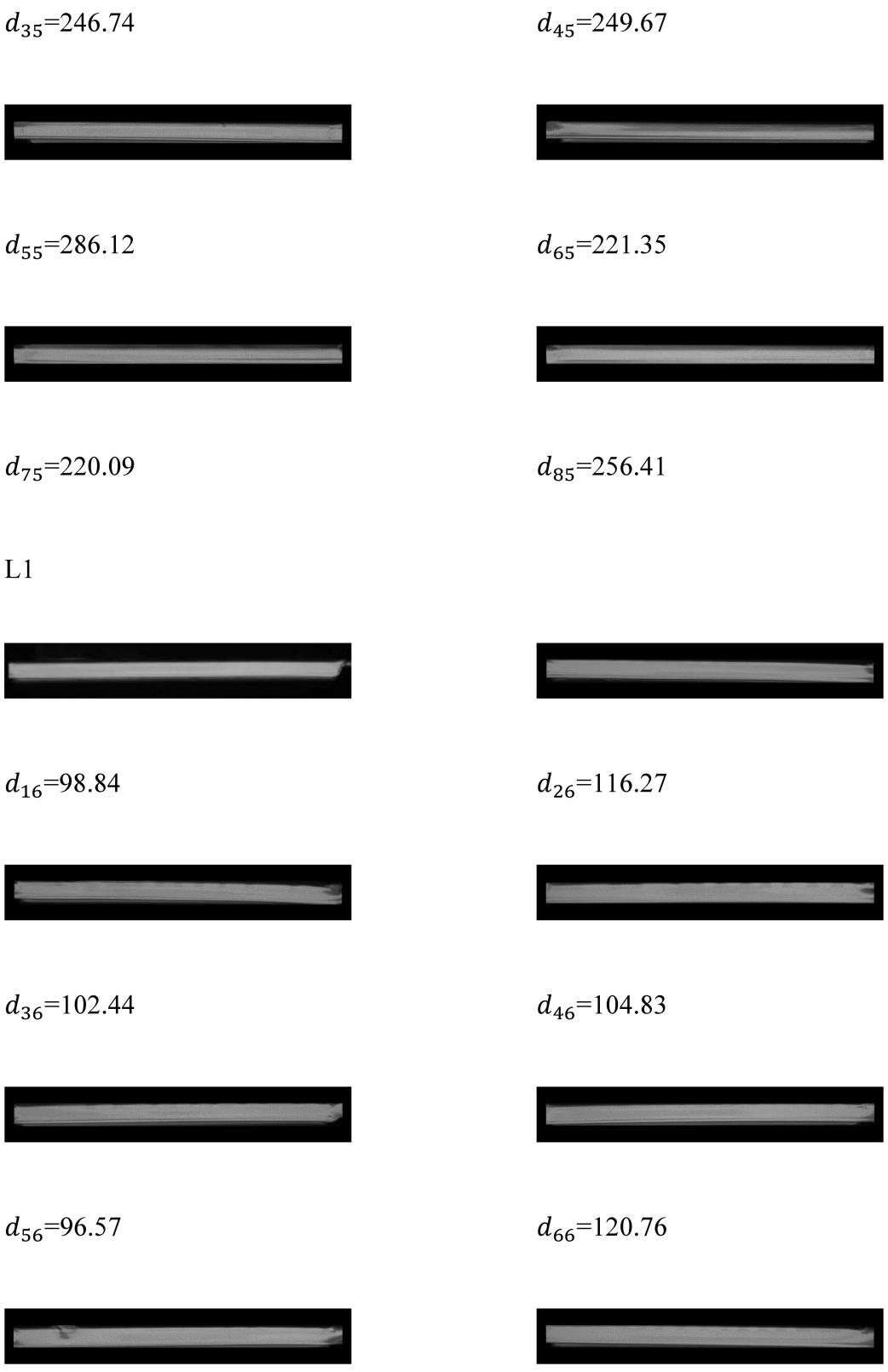

Figure 17. Continued

cells. The experimental results are shown in Fig. 18. The results indicate that the proposed method can realise the automatic transformation function of 7 calibration points of each cell to be detected. From the results shown in Fig. 18(a), it can be found that the clarity range of automatic correction and positioning in the left corner (CL) is within the interval [100.07, 136.93]. According to the actual production line data, when the CL resolution target value is not less than 100, it can meet the demand for automatic replacement of the production line. So the MOIR can smoothly carry out deviation correction and positioning and stable online real-time detection.

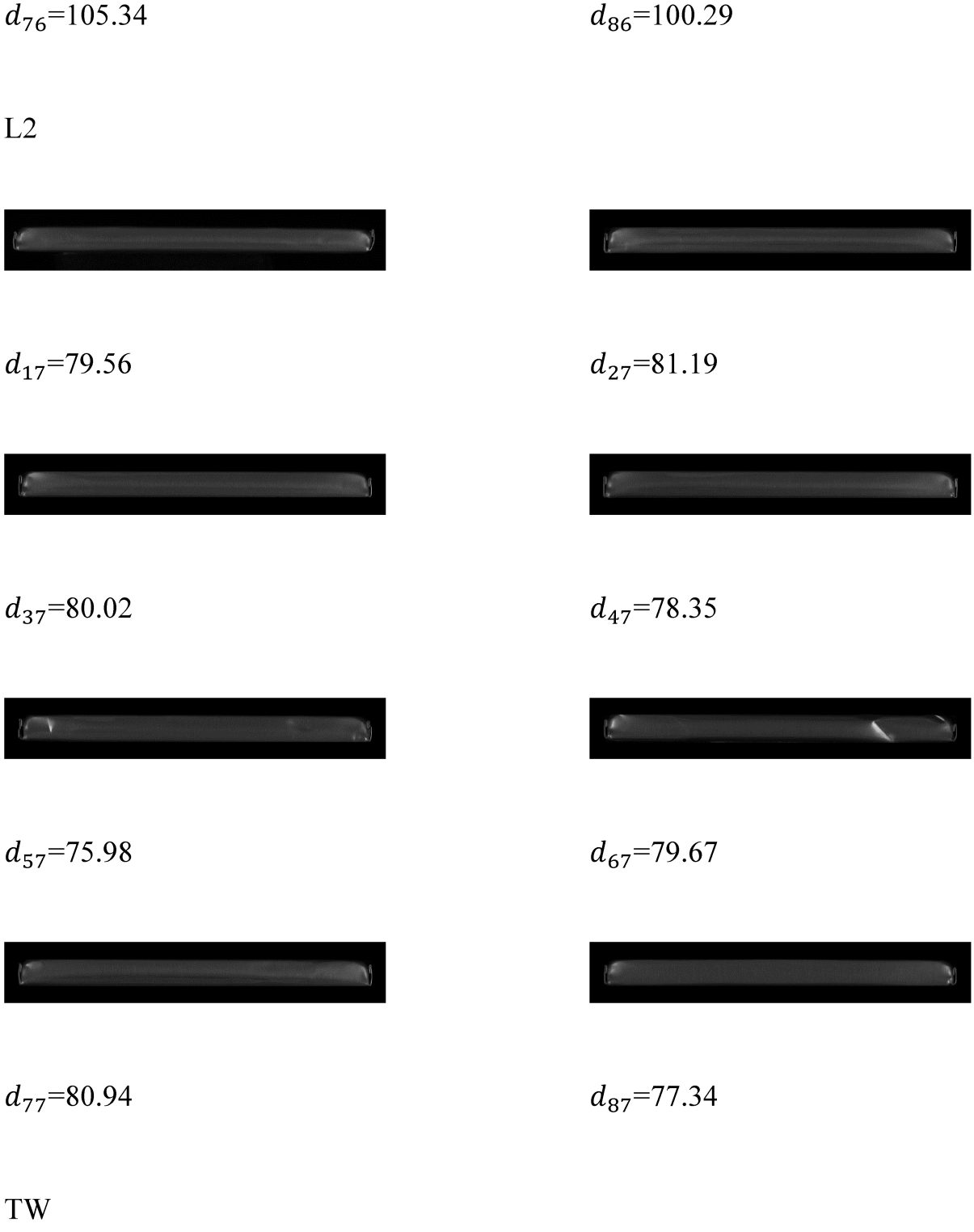

Figure 17. Continued

According to the same analysis, the clarity ranges of CR, L1, L2, HL, HR, and TW of the battery cells are [131.39, 181.80], [188.25, 299.74], [91.03, 124.69], [846.31, 1095.27], [610.91, 851.43], [71.34, 102.4], respectively.

A large number of practical examples prove that in the actual production process, the MOIR designed in this paper needs to separately satisfy the corresponding target clarity values of 100,130, 180, 90, 850, 600, 70 for different detection positions of different lithium-ion battery cell types, to successfully realise multi-scene automatic transformation, and meet the rapid mass production of automatic production lines.

From the analysis of the results shown, it can be seen that in the same location to be detected, the resolution values corresponding to different lithium-ion battery cells are not the same. The main reason is that different models of lithium-ion battery cells have different dimensions and different colors, different types of light sources, such as

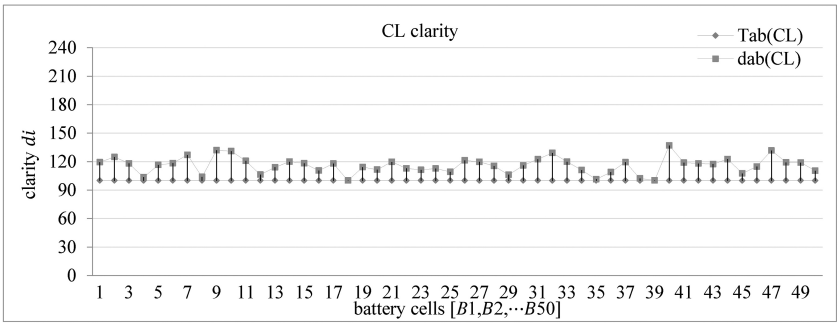

(a)

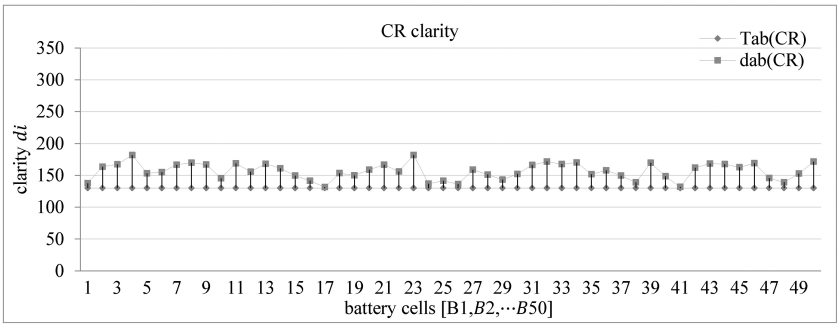

(b)

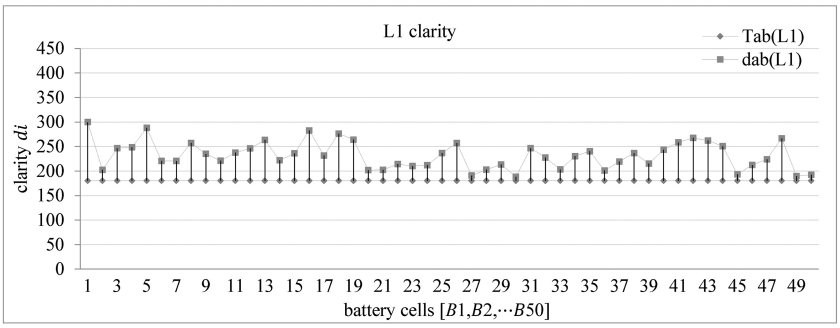

(c)

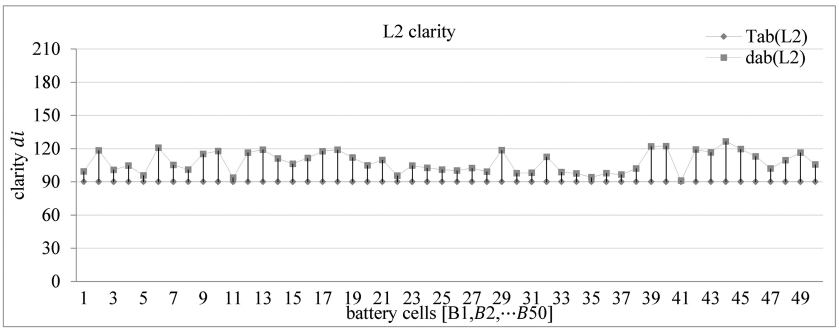

(d)

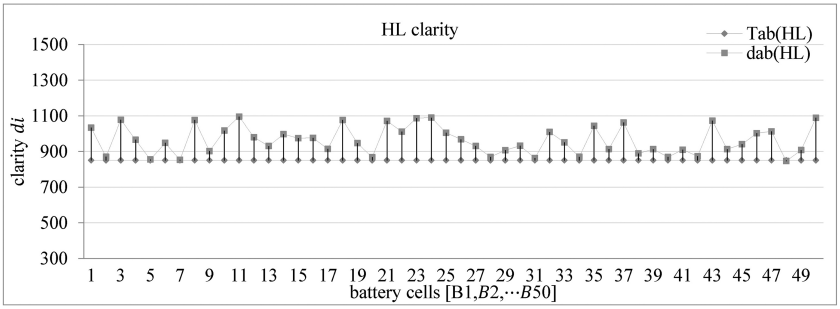

(e)

Figure 18. Clarity results of multi-scene automatic transformation.

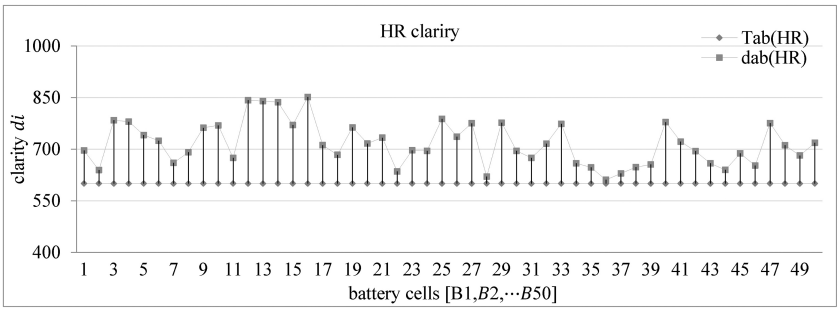

(a)

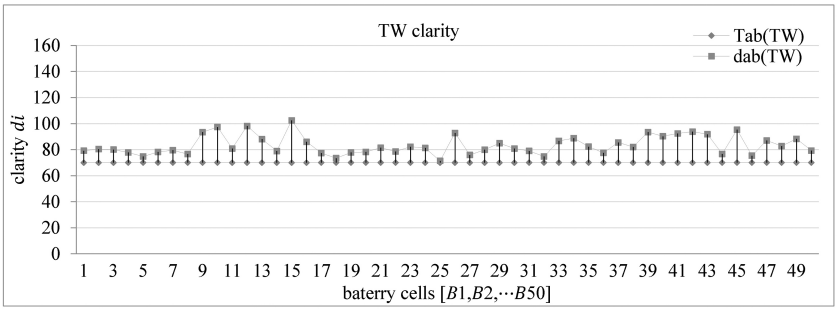

(b)

Figure 18. Continued

Table 2
The System Repeated Reliability Results of ACP Method

NO.	MOIRs	R_{it}(CL)	R_{it}(CR)	R_{it}(L1)	R_{it}(L2)	R_{it}(HL)	R_{it}(HR)	R_{it}(TW)
1	R1	98.42%	108.05%	106.74%	106.44%	113.40%	106.36%	102.81%
2	R2	113.56%	111.65%	102.66%	101.42%	101.81%	104.97%	104.25%
3	R3	101.98%	106.86%	111.09%	99.18%	106.91%	97.09%	105.53%
4	R4	115.22%	99.04%	99.55%	101.36%	103.39%	103.55%	103.41%
5	R5	108.73%	102.73%	104.17%	106.66%	108.82%	109.31%	99.06%
6	R6	109.72%	102.57%	106.62%	105.72%	109.11%	109.02%	95.82%
7	R7	107.92%	109.34%	113.19%	105.30%	103.43%	114.55%	106.46%
8	R8	96.39%	107.17%	98.34%	100.39%	103.96%	98.79%	102.25%
R_{rsd}		106.49%	105.93%	105.29%	103.31%	106.35%	105.45%	102.45%

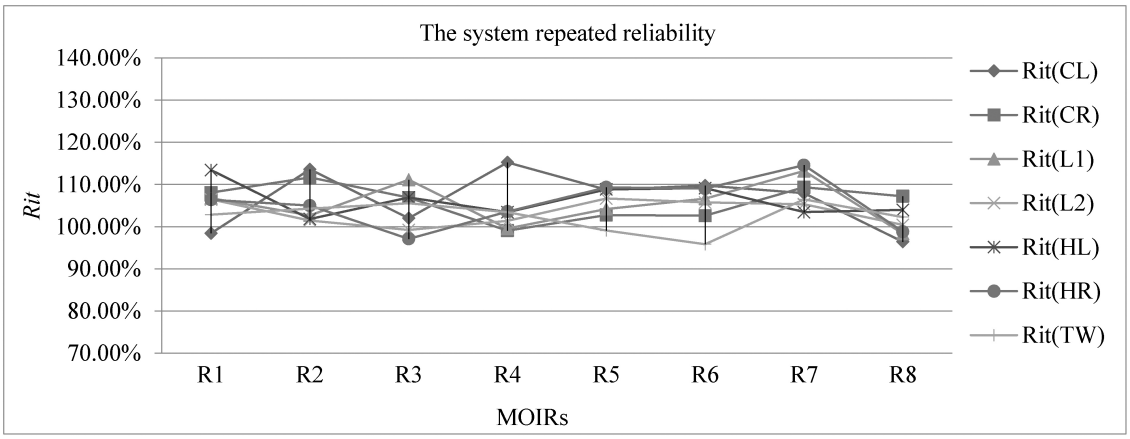

Figure 19. The system repeated reliability chart of ACP method.

Table 3
The System Compatible Reliability Results of ACP

No.	MOIRs	R_{ab}(CL)	R_{ab}(CR)	R_{ab}(L1)	R_{ab}(L2)	R_{ab}(HL)	R_{ab}(HR)	R_{ab}(TW)
1	R1	98.73%	102.33%	100.92%	102.53%	101.24%	99.23%	102.23%
2	R2	100.23%	100.44%	100.43%	99.06%	100.09%	100.35%	100.13%
3	R3	99.52%	101.86%	99.82%	100.25%	100.02%	99.93%	99.10%
4	R4	100.51%	100.02%	99.96%	99.83%	99.67%	100.33%	101.00%
5	R5	99.72%	99.84%	100.10%	99.67%	100.02%	99.95%	100.41%
6	R6	101.99%	99.92%	100.23%	99.58%	99.54%	99.58%	100.31%
7	R7	100.28%	99.21%	99.80%	99.80%	98.63%	100.17%	98.88%
8	R8	100.19%	100.01%	100.56%	99.77%	99.97%	99.98%	100.82%
R_{comp}		100.15%	100.46%	100.23%	100.06%	99.90%	99.94%	100.36%

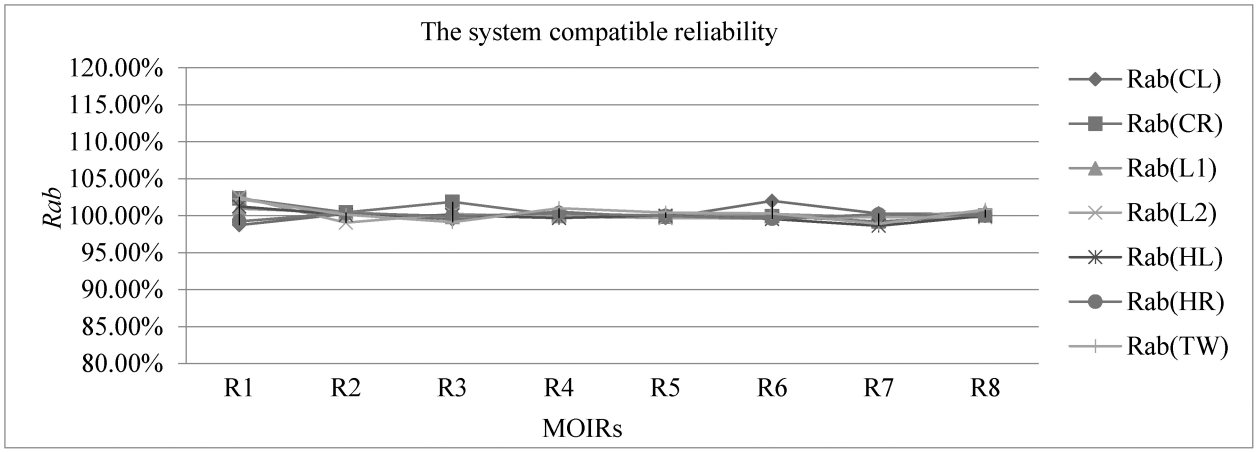

Figure 20. The system compatible reliability chart of ACP method.

violet light, infrared light, white light, green light, *etc.* should be used, so the average grey value generated after taking photos is not the same. This results in a difference in clarity values.

And in the same type of lithium-ion battery cell, the clarity value varies with the detection locations. As the angle, the shape, and the target to be detected are different in different locations, the same light source cannot satisfy the lighting needs of all detection conditions. Different models and light sources of different light types need to be combined and matched, resulting in different clarity values.

From the analysis of the experimental results, it can be seen that aim at the experimental objects and conditions of 50 kinds of lithium-ion battery cells used in this paper, the proposed method in this paper can realise the automatic transformation function of MOIR on the actual production line.

4.2 Repeated Reliability Results Analysis

In order to verify the system repeated reliability of the proposed method, one of the target battery cells was randomly selected to test. Table 2 and Fig. 16 show the experimental analysis results. The system repeated ACP reliability R_{rsd} of 8 MOIRs for 7 detection points in the target battery cell are, respectively, 106.49%, 105.93%, 105.29%, 103.31%, 106.35%, 105.45%, and 102.45%. And according to the actual production data results can be known that when the repeated reliability accuracy R_{abD} is no less than 95%, the MOIRs can accurately realise the target of automatic transformation. From this result, it can be seen that the multi-scene ACP method proposed in this paper has high system repeated reliability.

4.3 Compatible Reliability Results Analysis

In this experiment, 50 kinds of target battery cells were tested for the system compatible reliability of ACP method. Table 3 and Fig. 17 show the analysis results of the experiments according to the evaluation methods proposed in this paper. From the analysis of the results, it can be seen that the R_{comp} of the system compatibility of 8 MOIRs for 7 detection points in 50 types of target objects are 100.15%, 100.46%, 100.23%, 100.06%, 99.90%, 99.94%, and 100.36%, respectively. According to the actual production results, we know that when the reliability of compatible is

no less than 95%, the MOIRs can accurately achieve the target of compatible changeover. This practical engineering application experiment result indicates that the proposed multi-scene ACP method has high reliability of system compatible.

5. Discussion and Conclusions

The unique characteristic of the proposed methodology is that it can solve the problem of ACP according to different specifications and features of new products online combine with the automatically clarity computing algorithm, so as to achieve the purpose of rapid changeover of production online. From the practical engineering application experimental results, it can be found that the ACP method has high accuracy, high efficiency, and strong system repeated reliability and compatible reliability. The technology proposed in this paper has been applied to the MOIRs for lithium-ion battery cells appearance defect detection production lines, and 138 sets of MOIRs have been successfully delivered to the customers for use as turnkey projects.

It should be pointed out that the proposed ACP method in conjunction with the clarity automatic recognition algorithm only be applied to the lithium-ion battery cell appearance defect detection field, and the clarity threshold value has a direct effect on the estimate of the algorithm. More or less, it is a matter of practical experience to properly choose. The method proposed in this study can be extended to handle more complex ACP of robot, but further experimental verification is needed for different cases and different fields. Our ongoing research is to achieve the method for automatically selecting a clarity threshold.

References

[1] E. Lyu, X. Yang, W. Liu, J. Wang, S. Song, and M.Q.-H. Meng, An autonomous eye-in-hand robotic system for picking objects in a supermarket environment with non-holonomic constraint, *International Journal of Robotics and Automation, 37*(4), 2022, 352–361.

[2] D. Hao, Application of neural networks for robot 3D mapping and annotation using depth image camera, *International Journal of Robotics and Automation, 37*(6), 2022, 431–436.

[3] L.D. Hanh and C.-Y. Lin, Autonomous gluing based on image-based visual servoing, *International Journal of Robotics and Automation, 36*(2), 2021, 119–127.

[4] Y. Feng, T. Tang, S. Chen, and Y. Wu, automated defect detection based on transfer learning and deep convolution generative adversarial networks, *International Journal of Robotics and Automation, 36*(6), 2021, 471–478.

[5] H. Zhang, W. Dong, C. Guo, S. Shu, and W. Zuo, A visual servo control system combining parallel structure with dual-lens zoom, *International Journal of Robotics and Automation, 34*(6), 2019, 231–240.

[6] A. Zeng, S. Song, K.-T. Yu, E. Donlon, F. R. Hogan, M.Bauza, D. Ma, O. Taylor, M. Liu, E. Romo, N. Fazeli, F. Alet, N. Chavan Dafle, R. Holladay, I. Morena, P. Qu Nair, D. Green, I. Taylor, W. Liu, T. Funkhouser, and A. Rodriguez, Robotic pick-and-place of novel objects in clutter with multi-affordance grasping and cross-domain image matching, *Proc. 2018 IEEE International Conf. on Robotics and Automation (ICRA)(IEEE, 2018)*, Brisbane, QLD, 1–8.

[7] W. Wu, X. Wang, D. Xu, and Y. Yin, Position and orientation measurement for autonomous aerial refueling based on monocular vision, *International Journal of Robotics and Automation, 32*, 2017, 4661–4672.

[8] X. Wu, Z. Li, and P. Wen, An automatic shoe-groove feature extraction method based on robot and structural laser scanning, *International Journal of Advanced Robotic Systems, 14*, 2017, 1–14.

[9] H. Abidi, M. Chtourou, K. Kaaniche, and H. Mekki, Saliency-based robust features for global visual servoing, *International Journal of Robotics and Automation, 31*(5), 2016, 390–395.

[10] B.P. Larouche and Z.H. Zhu, Position-based visual servoing in robotic capture of moving target enhanced by Kalman filter, *International Journal of Robotics and Automation, 30*(3), 2015, 267–277.

[11] Z. Liu, H. Chen, G. Feng, and D. Hu, Tracking objects using shape context matching, *Neurocomputing, 83*, 2012, 47–55.

[12] J. Xu, N. Xi, C. Zhang, J. Zhao, B. Gao, and Q. Shi, Rapid 3D surface profile measurement of industrial parts using two-level structured light patterns, *Optics and Lasers in Engineering, 49*, 2011, 907–914.

[13] I. Siradjiddin, L. Behera, T.M. McGinnity, and S. Coleman, Image based visual servoing of a 7 DOF robot manipulator using a distributed fuzzy proportional controller, *Proc. 2010 IEEE International Conf. on Fuzzy Systems*, Barcelona, Spain, 2010, 1–8.

[14] P. Zhao and N.H. Wang, Precise perimeter measurement for 3D object with a binocular stereovision measurement system, *Optik*, *121*, 2010, 953–957.

[15] E. Tatlicioglu, D.M. Dawson, and B. Xian, Adaptive visual servo regulation control for camera-in-hand configuration with a fixed camera extension, *International Journal of Robotics and Automation, 24*(4), 2009, 346–355.

[16] T.P. Pachidis and J.N. Lygouras, Vision-based path generation method for a robot-based arc welding system, *Journal of Intelligent and Robotic Systems, 48*, 2007, 307–331.

[17] Z. Hu, C. Marshall, R. Bicker, and P. Taylor, Automatic surface roughing with 3D machine vision and cooperative robot control, *Robotic and Autonomous Systems*, *55*, 2007, 552–560.

[18] Y. Fang, W.E. Dixon, D.M. Dawson, and J. Chen, An exponential class of visual servoing controllers in the presence of uncertain camera calibration, *International Journal of Robotics and Automation*, *21*(4), 2006, 247–254.

[19] P.A. Bender and G.M. Bone, Automated grasp planning and execution for real-world objects using computer vision and tactile probing, *International Journal of Robotics and Automation*, *19*(1), 2004, 15–27.

[20] J. Paul, A. Schmidt, and G. Sommer, Vision-based integrated system for object inspection and handling, *Robotic and Autonomous Systems*, *37*, 2001, 297–309.

Biographies

Chen De was born in China on March 14, 1986. He received the B.S. and M.S. degrees in mechanical manufacture and automation from China Three Gorges University, China, in 2011 and 2014. respectively. He is currently pursuing the Doctoral degree with the Beijing Institute of Technology. He currently works as the Deputy Dean with the Institute of Guangdong Lyric Robot Automation Co., Ltd., China. His research interests focus on the control of autonomous vehicles.

Yan Qingdong was born in China on November 09, 1964. He received the M.S. and Ph.D. degrees from Beijing Institute of Technology, China, in 1988 and 1995, respectively. After then, he is a Professor with the Dept. of Mechanical Engineering, Beijing Institute of Technology, Beijing, China. His research has been on engaged in investigation and teaching of hydraulic transmission.

Zhou Junxiong was born in China on December 12, 1971. He received the M.S. degree in computer science and technology in 1988. He currently works as the Chairman and a General Manager of Guangdong Lyric Robot Automation Co., Ltd., China, His research has been on mechanical and electronic engineering technology in intelligent manufacturing field.

Du Yixian was born in China on October 13, 1978. He received the M.S. degree in mechanical engineering from China Three Gorges University, China, in 2004 and the Ph.D. degree in digital design and manufacturing from Huazhong University of Science and Technology, China, in 2007. His fields of interest are lithium battery intelligent manufacturing, machine vision, intelligent control, and laser processing.

Wang Hai was born in China on June 28, 1989. He received the B.S. and M.S. degrees in mechanical manufacture and automation from Chongqing Jiaotong University, China, in 2014 and 2017, respectively. He currently works as a Research Assistant with the Institute of Guangdong Lyric Robot Automation Co., Ltd., China. His research interests focus on intelligent manufacturing.

Li Shipeng was born in China on September 09, 1988. He received the B.S., M.S., and Ph.D. degrees in mechanical manufacture and automation from South China University of Technology, China, in 2011, 2014, and 2021, respectively. He currently works as a Senior Manager with China International Marine Containers (Group) Ltd., China, and he is also a Postdoctoral Fellow with Zhejiang University. His research interests focus on robot visual servo, product intelligence, intelligent manufacturing, and machine vision.